

# Anomalous rheology of puller-type microswimmer suspensions

Haruki Hayano\* and Akira Furukawa†

*Institute of Industrial Science, University of Tokyo, Meguro-ku, Tokyo 153-8505, Japan*

(Dated: August 21, 2024)

We explore the mechanism behind the anomalous rheology of puller-type microswimmer suspensions through direct hydrodynamic simulations. Our simulations demonstrate that swimmers' orientations near boundary walls predominantly control the overall swimming states and the resultant rheological properties. Hydrodynamic interactions due to specific flow fields characteristic of pullers cause the swimmers to line up vertically, particularly close to the walls where swimmer density peaks, enhancing the polar order of collective motion. Furthermore, the swimming directions near the walls depend significantly on the aspect ratio of the swimmer's body: rod-like swimmers tend to swim toward the flow direction, while swimmers with spherical bodies swim against the flow direction. The present results contrast with our previous simulations of suspensions of pusher-type swimmers, where weak orientation order in bulk regions determines the steady-state properties. Furthermore, these findings highlight that the rheological properties of active suspensions vary widely depending on the swimmers' properties, such as their shapes and swimming mechanisms.

Unique rheological properties, absent in passive suspensions, have been observed in active suspensions [1–11]. For instance, in suspensions of *E. coli*, categorized as pusher-type microswimmers, viscosity decreases sharply below the solvent viscosity at relatively low concentrations and shear rates [2–6], frequently resulting in a superfluid state with zero viscosity [4, 6]. In contrast, in suspensions of *Chlamydomonas reinhardtii*, classified as puller-type microswimmers, a steeper increase in viscosity compared to non-motile cells has been experimentally observed [7, 8]. Such anomalies in viscosity were first predicted by a seminal phenomenological model proposed by Hatwalne *et al.* [1], suggesting that stress can vary due to the swimmers' self-propulsive forces when swimmers have orientational order under shear flow.

For rod-like particles, thermal or athermal rotational diffusion combined with shear flow produces weak orientational order [12, 13], with which self-propulsive forces can provide non-zero active stress [11]. However, the substantial origin of rotational diffusion and orientational order in active suspensions remains elusive. One potential candidate is hydrodynamic interactions (HIs) among constituent swimmers, which may significantly contribute to the rotational diffusion of rod-like swimmers [14, 15]. Recently, our hydrodynamic simulations [16] using model pusher-type swimmers designed to replicate *E. coli* suspensions reveal that, under shear flow, weak orientational order systematically evolves via hydrodynamic scattering during travel between boundary walls. The simulations also show that swimmers near the walls move in the forward-flow direction, which is an important characteristic of rod-like pusher-type swimmers [17–19]. Furthermore, in Ref. [16], we argue that even at around 1% concentrations of *E. coli*, HIs can dominate over other effects, such as thermal fluctuations, contributing signif-

icantly to the unusual behavior of active suspensions.

Meanwhile, as noted above, it has been experimentally observed that the viscosity of suspensions of motile *Chlamydomonas* is significantly larger than that of non-motile ones [7, 8], which contrasts with the case of pusher suspensions. However, it is not trivial, even qualitatively, to determine what steady-state swimming properties are responsible for such anomalous rheology distinct from those observed for pusher-type swimmers. Simulation studies by Jibuti *et al.* [20], in which a model swimmer with a spherical body and two beating spherical flagella replicating *Chlamydomonas* is used, show that due to the beating motions of flagella, the rotational motions of the swimmers are notably different from those of rod-like particles, leading to a significant increase in suspension viscosity. Although the simulation results and their physical implications are compelling, the potential influence of many-body HIs, which can greatly impact steady-state behaviors, should be further investigated. Additionally, in actual experimental systems, boundary walls exist, inevitably affecting the dynamics of swimmers and the flow field near walls. It is unclear how these effects influence overall rheological properties and how they differ from those of pusher-type swimmers.

In this study, we numerically address these problems through direct hydrodynamic simulations using model puller-type microswimmers. Our model swimmer is composed of a body and two flagellum parts. The body part is treated as a rigid body, while the flagellum parts are represented as two spherical massless particles simply following the body's motions. This treatment keeps the relative position of these body and flagellum parts unchanged. For the  $\alpha$ -th swimmer ( $\alpha = 1, \dots, N$ ), with  $N$  being the total number of swimmers, we assume that a force  $F_A \hat{n}_\alpha$  acting on the body is exerted by the flagellum parts and that each flagellum part also exerts the force  $-(1/2)F_A \hat{n}_\alpha$  directly on the solvent fluid. Here,  $\hat{n}_\alpha$  represents the direction of the  $\alpha$ -th swimmer. The present particle-based model, schematically shown in Fig. 1(a), is essentially the same as those proposed in Refs. [21, 22]

\*hayano@iis.u-tokyo.ac.jp

†furu@iis.u-tokyo.ac.jp

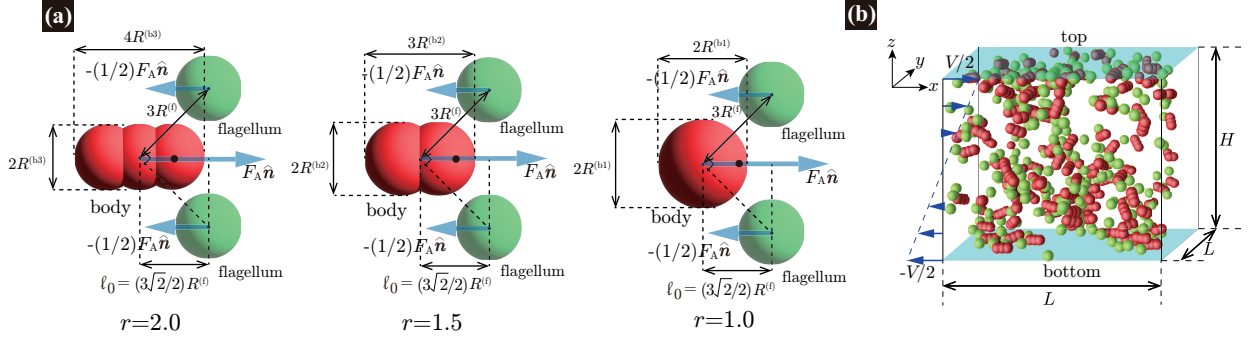


FIG. 1: (Color online) (a) The three different model swimmers contain "body" and "flagellum" parts. The body parts are composed of a superposition of 3-spheres, 2-spheres, and a single sphere with radii  $R^{(b3)}$ ,  $R^{(b2)}$ , and  $R^{(b1)}$ , respectively (from left to right). The radii of these spheres are set to make the resultant body volume, denoted as  $\mathcal{V}_b$ , the same for these three swimmer models. The corresponding aspect ratios  $r$  are 2.0, 1.5, and 1.0, respectively. The flagellum parts are composed of two spheres with radius  $R^{(f)} (= R^{(b3)})$ . The active force  $F_A \hat{\mathbf{n}}$  is exerted on the body, while  $-(F_A/2)\hat{\mathbf{n}}$  is directly exerted on the solvent through the two flagellum parts, with  $\hat{\mathbf{n}}$  representing the swimmer's orientation. As being sufficiently apart from the swimmer, it appears that a force dipole, which is constituted by these forces, with a magnitude of  $F_A \ell_0$ , exists at the point represented by the black circle. Here,  $\ell_0$  is the characteristic swimmer's length, which is given by  $\ell_0 = (3\sqrt{2}/2)R^{(f)}$  of the present model. More details of these swimmer models are described in the Supplementary Information (SI). (b) Our model suspension imposes periodic boundary conditions in the  $x$ - and  $y$ -directions with the linear dimension  $L$ . The shear flow is imposed by moving the top and bottom walls in the  $x$ -direction at constant velocities  $V/2$  and  $-V/2$ , respectively. These two walls are separated in the  $z$ -direction by the distance  $H$ .

and used in Refs. [14–16, 23–25]. Notably, in most of these former studies, it was supposed that the swimmers were of the pusher-type, while puller ones were employed in the current simulations. In this study, to address the effects of the swimmer's shape on rheological properties, we employed three different aspect ratios  $r = 1.0, 1.5$ , and  $2.0$  with the same volume  $\mathcal{V}_b$  for the body part, as illustrated in Fig. 1(a). On the other hand, for these three models, the flagellum parts are composed of two identical spheres of radius  $R^{(f)} (= R^{(b3)})$ . Periodic boundary conditions are imposed in the  $x$ - and  $y$ -directions with the linear dimension  $L$ , and the planar top and bottom walls are placed at  $z = H/2$  and  $-H/2$ , respectively. The shear flow is imposed by moving the top and bottom walls in the  $x$ -direction at constant velocities of  $V/2$  and  $-V/2$ , respectively, whereby the mean shear rate is  $\dot{\gamma} = V/H$ . In our simulations, HIs among the constituent swimmers are incorporated by adopting the smoothed profile method (SPM) [26–28], which is one of the mesoscopic simulation techniques [29–33]. More details of the model and simulations are provided in the Supplemental Information (SI).

Next, the simulation results are presented. First, in Fig. 2, we show the viscosity  $\eta$  under various conditions. In this study, the viscosity is defined as

$$\eta = \frac{1}{\dot{\gamma} L^2} \int dx dy \langle \Sigma_{xz}(x, y, \pm H/2) \rangle, \quad (1)$$

where  $\Sigma_{xz}(x, y, \pm H/2)$  is the  $xz$  component of the stress tensor at the walls and  $\langle \dots \rangle$  hereafter denotes the time average at a steady-state. Here, the solvent viscosity

is scaled to be 1. We find that  $\eta$  increases with increasing  $\phi$  for all aspect ratios  $r$ . For elongated swimmers ( $r = 2.0, 1.5$ ), the viscosity is higher than the solvent viscosity for all  $\phi$ , aligning with experimental results for *Chlamydomonas* suspensions [7, 8]. In contrast, for spherical swimmers ( $r = 1.0$ ), the viscosity is lower than the solvent viscosity at  $\phi \lesssim 0.04$ . This behavior strongly depends on  $r$  and the volume fraction of the swimmers, defined as  $\phi = N\mathcal{V}^{(b)}/L^2H$ .

The viscosity can be divided into three parts:  $\eta = \eta_s + \Delta\eta_p + \Delta\eta_a$ , where  $\eta_s (= 1$  in this study) is the solvent viscosity,  $\Delta\eta_p$  and  $\Delta\eta_a$  are the passive and active contributions, respectively (see SI for more details). In the present framework,  $\Delta\eta_a$  is given as

$$\Delta\eta_a = \frac{1}{\dot{\gamma} L^2 H} F_A \ell_0 \sum_{\alpha=1}^N \langle \hat{n}_{\alpha,x}(t) \hat{n}_{\alpha,z}(t) \rangle, \quad (2)$$

where  $\hat{\mathbf{n}}_{\alpha}(t)$  is the unit vector representing the  $\alpha$ -th swimmer's orientation at time  $t$ , and  $\hat{n}_{\alpha,x}$  and  $\hat{n}_{\alpha,z}$  are its  $x$  and  $z$  components, respectively. Essentially identical expressions of Eq. (2) were previously derived (see Refs. [11, 23, 34] for example). From Eq. (2), when swimmers tend to align along the extension direction of the flow field ( $\langle \hat{n}_{\alpha,x} \hat{n}_{\alpha,z} \rangle > 0$ ),  $\Delta\eta_a > 0$ . It is noteworthy that for pusher-type swimmers, a minus sign is applied in Eq. (2); an opposite change takes place in the puller case.

To further investigate the swimming states involved in the anomalous viscosity, the following steady-state quantities were examined:  $\rho(z) = \sum_{\alpha=1}^N \langle \delta[\mathbf{r} - \mathbf{R}_{\alpha}(t)] \rangle$ ,  $\mathbf{p}(z) = \sum_{\alpha=1}^N \langle \hat{\mathbf{n}}_{\alpha}(t) \delta[\mathbf{r} - \mathbf{R}_{\alpha}(t)] \rangle$ , and  $\overleftrightarrow{\mathbf{W}}(z) =$

$\sum_{\alpha=1}^N \langle [\hat{\mathbf{n}}_{\alpha}(t) \hat{\mathbf{n}}_{\alpha}(t) - \overset{\leftrightarrow}{\delta} / 3] \delta[\mathbf{r} - \mathbf{R}_{\alpha}(t)] \rangle$ . Here,  $\mathbf{R}_{\alpha}(t)$  is the position corresponding to the black circles drawn in Fig. 1(a) (see also the caption),  $\rho(z)$  is the density, and  $\mathbf{p}(z)/\rho(z)$  and  $\overset{\leftrightarrow}{\mathbf{W}}(z)/\rho(z)$  represent the polarization vector and the nematic order parameter tensor, respectively [9]. These quantities are shown in Figs. 3(a)-(h) for various conditions. Here, the following points should be noted. The present puller model used here tends to produce large collective motions due to HIIs among the swimmers, with strong polar order and fluctuations of swimmer density, in particular for the case of  $r = 1.0$ . Therefore, although these quantities should ideally be symmetric with respect to  $z = 0$ , achieving this in practical simulations requires an extremely large number of samples and long-time averages. In fact, the larger the number of samples is, the closer the simulation is to the ideal situation. These points are discussed in the SI.

In Figs. 3(a) and (b),  $\rho(z)$  has significant peaks near the boundary walls, and otherwise, it is almost constant (except at higher  $\phi$ ), indicating that the walls effectively attract swimmers. Such behaviors have been previously reported and discussed in the literature (for example, Refs. [18, 19, 35–42]). Note that for  $r = 1.0$ , the symmetry of the  $z$ -axis is slightly disrupted, which is discussed in the SI.

Figures 3(c)-(f) display  $\mathbf{p}(z)/\rho(z)$ .  $p_z(z)/\rho(z)$  exhibits similar behavior regardless of the aspect ratio  $r$  and concentration  $\phi$ , indicating that swimmers temporarily trapped at the walls tend to tilt their "heads" toward the walls. This behavior has been previously reported for rod-like pusher swimmers (see, for example, Refs. [43–45]). On the other hand,  $p_x(z)/\rho(z)$  shows significant  $r$ -dependence: For swimmers with a rod-like body ( $r = 2.0$ ),  $p_x(z)/\rho(z)$  is positive for  $z > 0$ , and negative for  $z < 0$ , suggesting that the swimmers move along the flow direction on average, which becomes most noticeable around the walls. In contrast, swimmers with a spher-

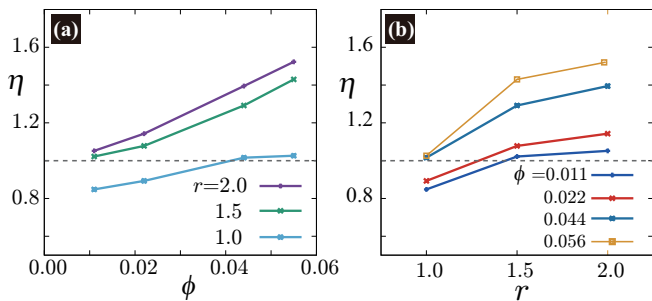


FIG. 2: (Color online) (a) The  $\phi$ -dependent viscosity for various aspect ratios  $r$  at  $H = 128$  and  $\dot{\gamma} = 10^{-3}$ . Our results indicate that  $\eta$  increases with increasing  $\phi$ , with the viscosity enhancement being much stronger at higher aspect ratios. (b) The  $r$ -dependence of the viscosity  $\eta$  for various  $\phi$  at  $H = 128$  and  $\dot{\gamma} = 10^{-3}$ . As  $r$  increases,  $\eta$  also increases. In both (a) and (b), the dashed lines indicate the solvent viscosity  $\eta_s (= 1)$ .

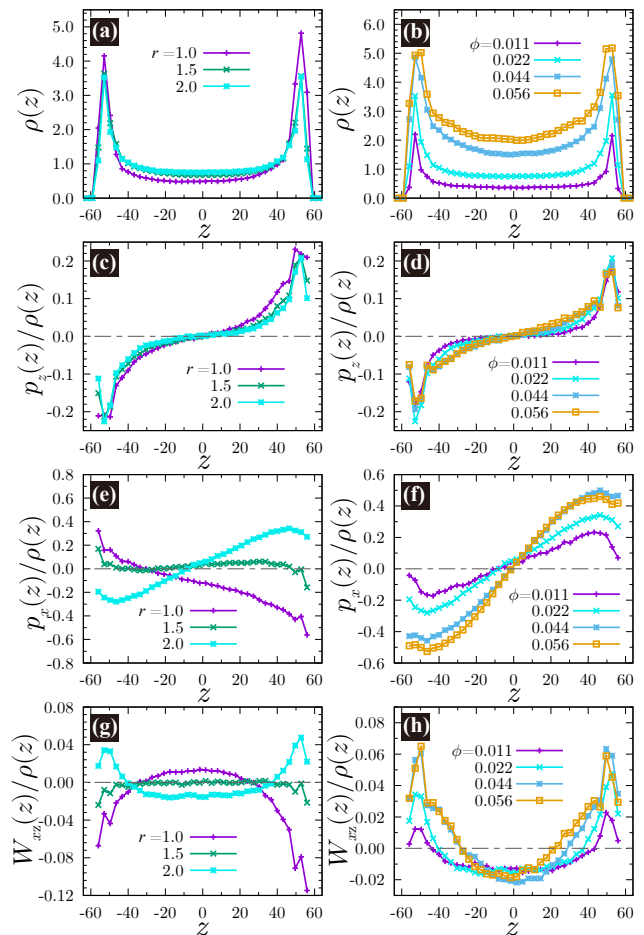


FIG. 3: (Color online) Subfigures (a), (c), (e), and (g) represent  $\rho(z)$ ,  $p_z(z)/\rho(z)$ ,  $p_x(z)/\rho(z)$ , and  $W_{xz}(z)/\rho(z)$ , respectively, for various values of  $r$  at  $\phi = 10^{-3}$ , and  $H = 128$ . On the other hand, subfigures (b), (d), (f), and (h) show the results for various values of  $\phi$  at  $r = 2.0$ ,  $\dot{\gamma} = 10^{-3}$ , and  $H = 128$ .

ical body ( $r = 1.0$ ) move in directions opposite to the mean flow direction on average, which is also most significant around the walls. At  $r = 1.5$ , a crossover between these two states takes place; a nearly flat  $z$ -dependence of  $p_x(z)/\rho(z)$  is observed in the bulk region, while the swimmers around the walls still show a tendency similar to that at  $r = 1.0$ .

In terms of viscosity enhancement or reduction, among Figs. 3(a)-(h), of particular interests are (g) and (h), exhibiting  $W_{xz}(z)/\rho(z)$ . For greater clarity, Eq. (2) is rewritten as

$$\Delta\eta_a = \frac{1}{\dot{\gamma}H} F_A \ell_0 \int_{-H/2}^{H/2} dz W_{xz}(z), \quad (3)$$

which shows that  $W_{xz}(z)$  is directly related to the viscosity enhancement/reduction. Distinct behaviors are observed between elongated swimmers and spherical swimmers. For  $r = 2.0$ ,  $W_{xz}(z)/\rho(z)$  is positive near the walls and slightly negative in the bulk region, and this trend

becomes more pronounced with increasing  $\phi$ . On the contrary, for  $r = 1.0$ ,  $W_{xz}(z)/\rho(z)$  is negative near the walls and positive in the bulk region. These results along with those in Fig. 2 suggest that the behaviors of  $W_{xz}(z)$  around the walls predominantly contribute to the viscosity enhancement (reduction) in the elongated (spherical) swimmers. For  $r = 1.5$ , an intermediate behavior between that at  $r = 2.0$  and  $r = 1.0$  is observed.

In Fig. 4(a), the  $x$ -component of the steady-state velocity field averaged over the  $xy$ -plane,  $\langle v_x \rangle(z)$ , is shown for  $r = 1.0, 1.5$ , and  $2.0$  at  $\phi = 0.022$ . Additionally,  $d\langle v_x \rangle(z)/dz$ , which is identical to the  $z$ -dependent solvent stress, is illustrated in Fig. 4(b). In the bulk region, the velocity gradient is enhanced and reduced at  $r = 2.0$  and  $1.0$ , respectively. On the other hand, near the walls, significantly negative velocity gradients and downward peaks in the solvent stress are observed for  $r = 2.0$ , while the opposite occurs for  $r = 1.0$ . Note that, in both the bulk and wall regions, at  $r = 1.5$ , the observed change in  $d\langle v_x \rangle(z)/dz$  is much smaller than those at  $r = 2.0$  and  $1.0$ . The viscosity observed at the walls results purely from solvent velocity gradients because the swimmers are not located in the narrow region near the walls due to the repulsive forces from the walls. Thus, this enhanced (reduced) viscosity immediately indicates the accelerated (decelerated) shear flow at the walls. In Figs. 5(a) and (b), we schematically display how swimming state affects solvent flow for the case of  $r = 2.0$ . The following points are worth noting. In the present puller systems, significant orientational order is more apparent around the walls than in the bulk regions. Consequently, steady-state swimming properties near the walls predominantly determine the resultant viscosity [see Eq. (3)]. However, this tendency is completely different from the pusher case [16], where the swimming properties in the bulk region control rheology for similar situations. This difference can be attributed to the difference in swimming mechanisms, specifically to the induced velocity fields, between pusher and puller swimmers.

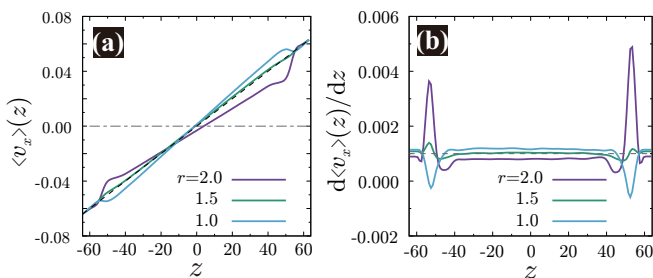


FIG. 4: (Color online) (a)  $\langle v_x \rangle(z)$ , averaged over the  $xy$ -plane for  $r = 1.0, 1.5, 2.0$  at  $\phi = 0.022$ . (b)  $d\langle v_x \rangle(z)/dz$  at the same condition as (a).

Finally, we discuss how the orientational and polar orders, shown in Fig. 3, are realized in the present model active suspension, and we attempt to deduce a possible description of global steady-states. To address this issue

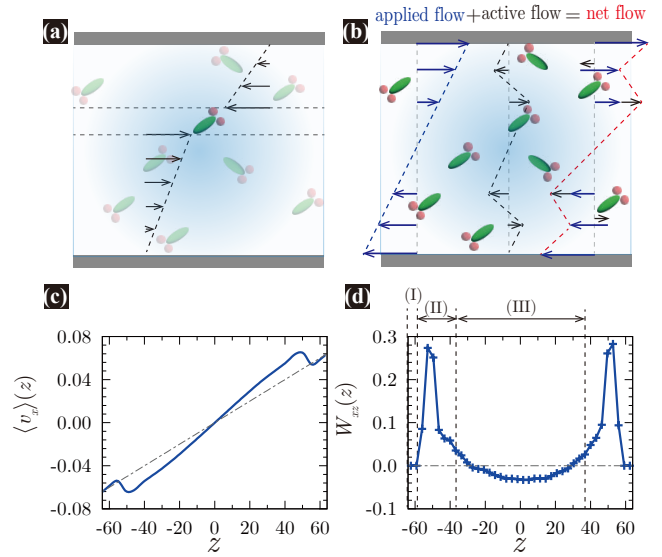


FIG. 5: (Color online) (a) For a swimmer, when  $\hat{n}_{\alpha,x}\hat{n}_{\alpha,z} > 0$ , the surrounding velocity gradient is weakened, while away from the swimmer, the opposite occurs. (b) The net flow is determined by a superposition of the individual swimmers' contributions.  $\langle v_x \rangle(z)$  (c) and  $W_{xz}(z)$  (d), at  $\phi = 0.044$ ,  $\dot{\gamma} = 10^{-3}$ , and  $H = 128$ . Near the walls, there are regions where a negative velocity gradient is observed, which closely corresponds to the region denoted as (II) [in (d)], where  $W_{xz}(z)$  shows significant positive peaks. To compensate for these negative velocity gradients in region (II), the velocity field is accelerated in regions (I) and (III).

in more detail, we introduce the following conditionally averaged density and polarization vector:

$$\rho^{\pm}(z) = \sum_{\alpha=1}^N \langle \delta[\mathbf{r} - \mathbf{R}_{\alpha}(t)] H(\pm \hat{n}_{\alpha,z}) \rangle, \quad (4)$$

$$\mathbf{p}^{\pm}(z) = \sum_{\alpha=1}^N \langle \hat{\mathbf{n}}_{\alpha}(t) \delta[\mathbf{r} - \mathbf{R}_{\alpha}(t)] H(\pm \hat{n}_{\alpha,z}) \rangle, \quad (5)$$

where  $H(x)$  is Heaviside's step function. In Eqs. (4) and (5), + and - denote that the summation is limited to swimmers with  $\hat{n}_z > 0$  and  $\hat{n}_z < 0$ , respectively.

Figures 6(a)-(d) show these quantities for  $r = 2.0$  and  $1.0$  at  $\phi = 0.022$ ,  $\dot{\gamma} = 10^{-3}$  and  $H = 128$ . As shown in Figs. 6(a) and (b),  $\rho^+(z)$  has large and small peaks near the top and bottom walls, respectively, while for  $\rho^-(z)$ , the opposite is observed. In the bulk region, these values are nearly constant. This behavior indicates that most swimmers near the walls tilt their "heads" toward the walls, while the swimmers tilting their "heads" toward the bulk region quickly escape from the wall regions. For  $r = 2.0$ , the differences between  $\rho^+(z)$  and  $\rho^-(z)$  near the walls are smaller than for  $r = 1.0$ , suggesting that rod-like ( $r = 2.0$ ) swimmers are more easily peeled off from the walls than spherical ( $r = 1.0$ ) ones. In Fig. 6(c),  $p_x^+(z)/\rho^+(z)$  and  $p_x^-(z)/\rho^-(z)$  are plotted. At  $r = 2.0$ , the average swimming directions are oriented along the

mean flow direction both for swimmers moving towards and away from the walls. Contrary to this, at  $r = 1.0$ , swimmers move against the mean flow direction. Additionally, Fig. 6(d) shows  $p_z^+(z)/\rho^+(z)$  and  $p_z^-(z)/\rho^-(z)$ , demonstrating that the swimmers moving towards the walls tend to orient vertically more than those moving away from the walls. This tendency is slightly enhanced for  $r = 2.0$  compared with  $r = 1.0$ .

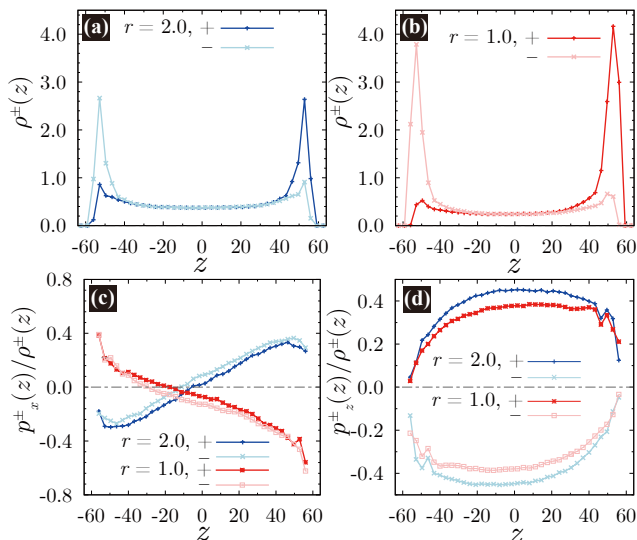


FIG. 6: (Color online) In (a) and (b),  $\rho^\pm(z)$  is shown for  $r = 2.0$  and  $1.0$ , respectively, at  $\phi = 0.022$ ,  $\dot{\gamma} = 10^{-3}$  and  $H = 128$ .  $p_x^\pm(z)/\rho^\pm(z)$  and  $p_z^\pm(z)/\rho^\pm(z)$  are shown in (c) and (d), respectively, under the same condition as (a) and (b).

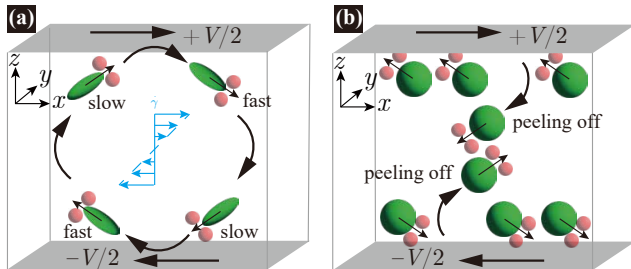


FIG. 7: (Color online) Schematic illustrations of the global steady-states for swimmers at  $r = 2.0$  (a) and  $r = 1.0$  (b). (a) For  $r = 2.0$ , the swimmers moving towards and away from walls orientate along the flow direction on average. (b) For  $r = 1.0$ , the swimmers near the walls tend to move against the flow direction on average, which make the swimmers stay around the walls for longer than those with  $r = 2.0$ . For further discussion, please refer to the main text.

As schematically shown in Fig. 7, rod-like swimmers ( $r = 2.0$ ), whether moving toward or away from the walls, tend to align with the flow direction. In contrast, swimmers with spherical bodies ( $r = 1.0$ ) tend to move against the flow direction and remain near the walls longer than those with  $r = 2.0$ , resulting in a higher swimmer density

around the walls. The key factor in understanding these behaviors is the competing effects of torques from the shear flow in the  $xy$ - and  $xz$ -planes. The torque in the  $xz$ -plane induces clockwise rotation in the swimmers. For swimmers moving opposite to the flow direction around the walls, further rotation is hindered by wall repulsion, acting as a counter torque to the shear flow. However, for swimmers moving along the flow direction, this steric hindrance is absent, allowing the  $xz$ -plane torque to orient them toward the bulk region, enabling escape from the walls. Meanwhile, the torque in the  $xy$ -plane aligns swimmers tilting toward the walls with the flow direction, a phenomenon known as the "weathercock effect." For rod-like swimmers, the influence of the  $xy$ -plane torque may be more significant than that due to the  $xz$ -plane torque, whereas for spherical swimmers, the latter one is weaker. This difference in the torque effect may explain why rod-like and spherical swimmers exhibit opposite tendencies in the moving directions. However, it is worth mentioning the following: the present puller swimmers tend to line up vertically due to HIs, frequently generating collective motions with polar orders (shown in SI). Such accompanying vertical motions seem to be geometrically more stable for shorter-body swimmers and persist for longer durations. These collective effects may significantly influence the determination of swimming direction more than the simple torque effects described above.

In this study, we investigated the steady-state swimming properties and associated viscosity changes for model puller-type microswimmers under various conditions. Although our models were designed to mimic *Chlamydomonas* by adjusting the shapes and relative positions of the swimmer body and flagellum parts, the simulation results show greater variation than the experimental observations, depending on the aspect ratio of the swimmer's bodies. Swimming direction near walls depends significantly on the aspect ratio of the swimmer's bodies. Rod-like swimmers tend to swim toward the flow direction, resulting in an increase in suspension viscosity. On the other hand, swimmers with spherical bodies swim against the flow direction, leading to a decrease in suspension viscosity. The present results contrast with our previous simulations of suspensions of pusher-type swimmers, where weak orientation order in bulk regions determines steady-state properties [16]. Additionally, for the present puller systems, polar and orientational orders are more pronounced than those for pusher swimmers under similar conditions (compare Fig. 3 with Fig. 3 in Ref. [16]), which may occur because the puller-type model swimmers tend to line up vertically due to HIs, bringing their "heads" and "tails" closer. Such polar order has been reported for squirmers in previous studies [46, 47]. These findings strongly indicate that the rheological properties of active suspensions vary widely depending on the swimmers' properties, such as their shapes and swimming mechanisms.

Finally, we address the discrepancy with experimental results. As noted above, the present model puller swim-

mers were designed to replicate actual *Chlamydomonas*, which is rather spherical. The experiments [7, 8] report an anomalous increase in viscosity, while our simulations show the opposite tendency for spherical puller swimmers. This discrepancy suggests the potential importance of the flagellum's beating motions, which generate self-propulsive forces. However, in our simulations, active forces are represented by constant prescribed ones. Differences in several conditions between the experiments [7, 8] and our simulations may also explain this discrepancy. In the experiments, the applied shear rate  $\dot{\gamma}$  is comparable to or larger than the intrinsic shear rate given by the swimmer's velocity divided by the swimmer's size. In the present simulations, on the other hand,  $\dot{\gamma}(= 10^{-3})$

is nearly ten times smaller than the intrinsic shear rate. Moreover, the volume fraction in our simulations is at most 0.056, while it is higher in the experiments. Other factors differing from experimental conditions, such as the system size, may also contribute. We will investigate these issues in future studies.

### Acknowledgments

This work was supported by JSPS KAKENHI (Grants No. 20H05619) and JST SPRING (Grants No. JP-MJSP2108).

- 
- [1] Y. Hatwalne, S. Ramaswamy, M. Rao, and R. A. Simha, Rheology of Active-particle suspensions, *Phys. Rev. Lett.* **92**, 118101 (2004).
- [2] A. Sokolov and I. S. Aranson, Reduction of viscosity in suspension of swimming bacteria, *Phys. Rev. Lett.* **103**, 148101 (2009).
- [3] J. Gachelin, G. Miño, H. Berthet, A. Lindner, A. Rouselet, and E. Clément, Non-Newtonian viscosity of *Escherichia coli* suspensions, *Phys. Rev. Lett.* **110**, 268103 (2013).
- [4] H. M. López, J. Gachelin, C. Douarche, H. Auradou, and E. Clément, Turning bacteria suspensions into superfluids, *Phys. Rev. Lett.* **115**, 028301 (2015).
- [5] A. Liu, K. Zhang, and X. Cheng, Rheology of bacterial suspensions under confinement, *Rheologica Acta* **58**, 439 (2019).
- [6] V.A. Martinez, E. Clément, J. Arlt, C. Douarche, A. Dawson, J. Schwarz-Linek, A.K. Creppy, V. Škultéty, A.N. Morozov, H. Auradou, and W.C.K. Poon, Symmetric shear banding and swarming vortices in bacterial superfluids, *Proc. Natl. Acad. Sci. U.S.A.* **117** 2326 (2020).
- [7] S. Rafaï, L. Jibuti, and P. Peyla, Effective viscosity of microswimmer suspensions, *Phys. Rev. Lett.* **104**, 098102 (2010).
- [8] M. Mussler, S. Rafaï, P. Peyla and C. Wagner, Effective viscosity of non-gravitactic *Chlamydomonas Reinhardtii* microswimmer suspensions, *EuroPphys. Lett.* **101** 54004 (2013).
- [9] M.C. Marchetti, J.F. Joanny, S. Ramaswamy, T.B. Liverpool, J. Prost, M. Rao, and R. A. Simha, Hydrodynamics of soft active matter, *Rev. Mod. Phys.* **85**, 1143 (2013).
- [10] M.C. Marchetti, Frictionless fluids from bacterial teamwork, *Nature* **525**, 37 (2015).
- [11] D. Saintillan, Rheology of active fluids, *Annu. Rev. Fluid Mech.* **50**, 563 (2018).
- [12] E.J. Hinch and L.G. Leal, The effect of Brownian motion on the rheological properties of a suspension of non-spherical particles, *J. Fluid Mech.* **52**, 683 (1972).
- [13] E.J. Hinch and L.G. Leal, Constitutive equations in suspension mechanics. Part 2. Approximate forms for a suspension of rigid particles affected by Brownian rotations, *J. Fluid. mech.* **76**, 187 (1976).
- [14] S.D. Ryan, B.M. Haines, L. Berlyand, F. Ziebert, and I.S. Aranson, Viscosity of bacterial suspensions: Hydrodynamic interactions and self-induced noise, *Phys. Rev. E* **83**, 050904(R) (2011).
- [15] V. Gyrya, I. S. Aranson, L. V. Berlyand, and D. Karpeev, A Model of Hydrodynamic Interaction Between Swimming Bacteria, *Bull. Math. Biol.* **72**, 148 (2010).
- [16] H. Hayano and A. Furukawa, Hydrodynamic interactions in anomalous rheology of active suspensions, *Phys. Rev. Research* **4**, 043091 (2022).
- [17] T. Kaya and H. Koser, Direct Upstream Motility in *Escherichia coli*, *Biophys. J.* **102**, 1514 (2012).
- [18] A.P. Berke, L. Turner, H.C. Berg, and E. Lauga, Hydrodynamic Attraction of Swimming Microorganisms by Surfaces, *Phys. Rev. Lett.* **101**, 038102 (2008).
- [19] G. Li and J.X. Tang, Accumulation of Microswimmers near a Surface Mediated by Collision and Rotational Brownian Motion, *Phys. Rev. Lett.* **103**, 078101 (2009).
- [20] L. Jibuti W. Zimmermann, S. Rafaï and P. Peyla, Effective viscosity of a suspension of flagellar-beating microswimmers: Three-dimensional modeling, *Phys. Rev. E* **96**, 052610 (2017).
- [21] J. P. Hernandez-Ortiz, C. G. Stoltz, and M. D. Graham, Transport and Collective Dynamics in Suspensions of Confined Swimming Particles, *Phys. Rev. Lett.* **95**, 204501 (2005).
- [22] P. T. Underhill, J. P. Hernandez-Ortiz, and M. D. Graham, Diffusion and Spatial Correlations in Suspensions of Swimming Particles, *Phys. Rev. Lett.* **100**, 248101 (2008).
- [23] B.M. Haines, A. Sokolov, I.S. Aranson, L. Berlyand, and D.A. Karpeev, Three-dimensional model for the effective viscosity of bacterial suspensions, *Phys. Rev. E* **80**, 041922 (2009).
- [24] A. Decoene, S. Martin, and B. Maury, Microscopic modeling of active bacterial suspensions, *Math. Model. Nat. Phenom.* **6**, 98 (2011).
- [25] A. Furukawa, D. Marenduzzo, and M.E. Cates, Activity-induced clustering in model dumbbell swimmers: The role of hydrodynamic interactions, *Phys. Rev. E* **90**, 022303 (2014).
- [26] Y. Nakayama and R. Yamamoto, Simulation method to resolve hydrodynamic interactions in colloidal dispersions, *Phys. Rev. E.* **71**, 036707 (2005).
- [27] J. J. Molina, K. Otomura, H. Shiba, H. Kobayashi, M. Sano, and R. Yamamoto, Rheological evaluation of col-

- loidal dispersions using the smoothed profile method: formulation and applications, *J. Fluid Mech.* **792**, 590 (2016).
- [28] R. Yamamoto, J. J. Molina, and Y. Nakayama, Smoothed profile method for direct numerical simulations of hydrodynamically interacting particles, *Soft Matter* **17**, 4226 (2021).
- [29] A.J.C. Ladd, Short-time motion of colloidal particles - numerical-simulation via a fluctuating lattice-Boltzmann equation, *Phys. Rev. Lett.* **70**, 1339 (1993).
- [30] M. E. Cates, K. Stratford, R. Adhikari, P. Stainsell, J.-C. Desplat, I. Pagonabarraga, and A.J. Wagner, Simulating colloid hydrodynamics with lattice Boltzmann methods, *J. Phys.: Condens. Matter* **16**, S3903 (2004).
- [31] H. Tanaka and T. Araki, Simulation Method of Colloidal Suspensions with Hydrodynamic Interactions: Fluid Particle Dynamics, *Phys. Rev. Lett.* **85**, 1338 (2000).
- [32] P. Español and P. Warren, Statistical Mechanics of Dissipative Particle Dynamics, *Europhys. Lett.* **30**, 191 (1995).
- [33] S. Ji, R. Jiang, R.G. Winkler, and G. Gompper, Mesoscale hydrodynamic modeling of a colloid in shear-thinning viscoelastic fluids under shear flow, *J. Chem. Phys.* **135** 134116 (2011).
- [34] D. Saintillan, The dilute rheology of swimming suspensions: A simple kinetic model, *Exp Mech* **50**, 1275 (2010).
- [35] E. Lauga and T.R. Powers, The hydrodynamics of swimming microorganisms, *Rep. Prog. Phys.* **72**, 096601 (2009).
- [36] E. Lauga, *The Fluid Dynamics of Cell Motility* (Cambridge University Press, Cambridge 2020).
- [37] N. Figueroa-Morales, G. L. Miño, A. Rivera, R. Caballero, E. Clément, E. Altshuler, and A. Lindner, Living on the edge: transfer and traffic of *E. coli* in a confined flow, *Soft Matter* **11**, 6284 (2015).
- [38] S. Bianchi, F. Saglimbeni, and R. Di Leonardo, Holographic Imaging Reveals the Mechanism of Wall Entrapment in Swimming Bacteria, *Phys. Rev. X* **7**, 011010 (2017).
- [39] P. Denissenko, V. Kantsler, D.J. Smith, and J. Kirkman-Brown, Human spermatozoa migration in microchannels reveals boundary-following navigation, *Proc. Natl. Acad. Sci. U.S.A.* **109**, 8007 (2012).
- [40] B. Ezhilan, R. Alonso-Matilla, and D. Saintillan, On the distribution and swim pressure of run-and-tumble particles in 50 confinement, *J. Fluid Mech.* **781**, R4 (2015).
- [41] B. Ezhilan and D. Saintillan, Transport of a dilute active suspension in pressure-driven channel flow, *J. Fluid Mech.* **777**, 482 (2015).
- [42] W. Yan and J.F. Brady The force on a boundary in active matter, *J. Fluid Mech.* **785**, R1 (2015).
- [43] M. A.-S. Vigeant, R. M. Ford, M. Wagner, and L. K. Tamm, Simplified modeling of *E. coli* mortality after genome damage induced by UV-C light exposure, *Appl. Environ. Microbiol.* **68**, 2794 (2002).
- [44] S.E. Spagnolie and E. Lauga, Hydrodynamics of self-propulsion near a boundary: predictions and accuracy of far-field approximations, *J. Fluid Mech.* **700**, 105 (2012).
- [45] O. Sipoș, K. Nagy, R. Di Leonardo, and P. Galajda, Hydrodynamic Trapping of Swimming Bacteria by Convex Walls, *Phys. Rev. Lett.* **114**, 258104 (2015).
- [46] A. A. Evans, T. Ishikawa, T. Yamaguchi, and E. Lauga, Orientational order in concentrated suspensions of spherical microswimmers, *Phys. of Fluids* **23**, 111702 (2011).
- [47] F. Alarcón, I. Pagonabarraga, Spontaneous aggregation and global polar ordering in squirmers suspensions, *J. Molecular Liquids* **185**, 56 (2013).